NRC·CNRC

NRC Publications Archive
Archives des publications du CNRC

Laser-produced craters in minerals of a palladium ore sample

Selmani, Samira; Elhamdaoui, Ismail; Mohamed, Nessrine; Bouchard, Paul; Constantin, Marc; Sabsabi, Mohamad; Vidal, François

This publication could be one of several versions: author's original, accepted manuscript or the publisher's version. / La version de cette publication peut être l'une des suivantes : la version prépublication de l'auteur, la version acceptée du manuscrit ou la version de l'éditeur.
For the publisher's version, please access the DOI link below./ Pour consulter la version de l'éditeur, utilisez le lien DOI ci-dessous.

Publisher's version / Version de l'éditeur:
https://doi.org/10.1007/s00339-023-06966-7
Applied Physics A, 129, 11, 2023-10-30

NRC Publications Archive Record / Notice des Archives des publications du CNRC :
https://nrc-publications.canada.ca/eng/view/object/?id=2471f892-2357-488d-9379-a1150f71c26a
https://publications-cnrc.canada.ca/fra/voir/objet/?id=2471f892-2357-488d-9379-a1150f71c26a

Access and use of this website and the material on it are subject to the Terms and Conditions set forth at
https://nrc-publications.canada.ca/eng/copyright
READ THESE TERMS AND CONDITIONS CAREFULLY BEFORE USING THIS WEBSITE.

L'accès à ce site Web et l'utilisation de son contenu sont assujettis aux conditions présentées dans le site
https://publications-cnrc.canada.ca/fra/droits
LISEZ CES CONDITIONS ATTENTIVEMENT AVANT D'UTILISER CE SITE WEB.

Questions? Contact the NRC Publications Archive team at PublicationsArchive-ArchivesPublications@nrc-cnrc.gc.ca. If you wish to email the authors directly, please see the first page of the publication for their contact information.

Vous avez des questions? Nous pouvons vous aider. Pour communiquer directement avec un auteur, consultez la première page de la revue dans laquelle son article a été publié afin de trouver ses coordonnées. Si vous n'arrivez pas à les repérer, communiquez avec nous à PublicationsArchive-ArchivesPublications@nrc-cnrc.gc.ca.

National Research Council Canada
Conseil national de recherches Canada
Canada

Applied Physics A (2023) 129:737
https://doi.org/10.1007/s00339-023-06966-7

Applied Physics A
Materials Science & Processing

Laser-produced craters in minerals of a palladium ore sample

Samira Selmani[1] · Ismail Elhamdaoui[1] · Nessrine Mohamed[2] · Paul Bouchard[3] · Marc Constantin[2] · Mohamad Sabsabi[3] · François Vidal[1]

Received: 16 June 2023 / Accepted: 28 August 2023 / Published online: 3 October 2023
© Crown 2023, corrected publication 2023

Abstract
Laser-induced breakdown spectroscopy (LIBS) is an emerging technique in geochemistry that allows rapid in-situ analysis of the elemental composition and concentration of minerals by laser ablation of the material surface and measurement of the light emitted by the resulting plasma. However, this type of application is still under development for geochemical analyses. Indeed, it is still difficult to know how minerals are ablated under laser pulses in the context of LIBS geochemical analysis using a high-power Q-switched Nd:YAG laser operating at 1064 nm with pulse durations on the order of nanoseconds. Important questions remain unanswered regarding the volume sampled by the laser beam on the minerals to be analyzed, as well as the plasmas induced by the laser on the minerals in air at atmospheric pressure. The objective of this work is to provide insight into laser-mineral interactions within the framework of LIBS geochemical analysis of ore samples with emphasis on the characterization of plasmas and laser ablation craters under ambient air at atmospheric pressure. We study the crater morphology in the three main phases of a palladium ore fragment (Lac des Iles mine, Canada), namely plagioclase feldspar, amphibole and sulfides [Mohamed et al., Geostand Geoanal Res 45:539, (2021)] We performed four series of laser shots (50, 250, 500 and 1000 shots) in the three mineral phases and characterized the morphology of the craters obtained by scanning electron microscopy and optical coherence tomography. It turns out that laser ablation is most effective in plagioclase, presumably due to its lower thermal conductivity. In addition, the temperature and electron density of the plasma were determined for each phase from the iron and nickel lines of LIBS spectra taken 4 µs after the laser shots. They are between 6300 and 8600 °C and about 2×10^{17} cm^{-3}, respectively.

Keywords Laser-Induced Breakdown Spectroscopy (LIBS) · Laser ablation · Plasma characterization · Mineral phases · Crater morphology

1 Introduction

Many characteristics of laser-induced breakdown spectroscopy (LIBS) make it an attractive analytical tool for the analysis of geological materials, both in the conventional laboratory and in the field [1–3]. LIBS is a simple yet versatile technique that can detect all chemical elements in any material with a sensitivity suitable for many applications. It requires little or no sample preparation; multi-element analysis of samples can be performed in real time; only a small portion of the sample is required for analysis; and it can detect trace and minor elements in a sample, which is important in many geological studies. Several studies have focused on the LIBS technique for applications in geological and environmental materials analysis [4–8]. By using calibration samples, it is possible to determine the concentration of elements present in samples of the same compositional family.

✉ Samira Selmani
Samira.Selmani@inrs.ca

✉ François Vidal
Francois.Vidal@inrs.ca

[1] Institut National de la Recherche Scientifique, Centre Énergie Matériaux Télécommunications, 1650 Lionel-Boulet blvd, Varennes, QC J3X 1P7, Canada

[2] Département de Géologie et de Génie Géologique, Université Laval, 1065 Avenue de la Médecine, Québec, QC G1V 0A6, Canada

[3] National Research Council of Canada, 75 de Mortagne Blvd., Boucherville, QC J4B 6Y4, Canada

Compared to LIBS, X-ray fluorescence (XRF) techniques suffer from a lack of sensitivity for light elements below Mg. Furthermore, in a portable format, XRF can hardly quantify traces of precious metals due to its low sensitivity and thus high detection limit [9]. As for infrared spectroscopy, it can determine the mineralogy of rock samples but not their elemental composition [10].

In LIBS analysis, a pulsed laser beam with a fluence that can range from a fraction to hundreds of J cm^{-2}, depending on the duration of the laser pulses (typically from tens of femtoseconds to a few nanoseconds) and the material to study, is focused on the sample surface, causing localized ablation of a very small amount (typically less than 1 mg) of the material. The ablated material initially forms a weakly ionized atomized plasma at high temperature (~20,000 K) which fairly well reflects the stoichiometry of the material [11] in the interaction zone. The plasma cools by increasing its volume and by emitting radiation on a time scale of typically a few microseconds. The plasma radiation consists of spectral lines from the de-excitation of atoms and ions, which are the unique signature of the elements present in the plasma, and a background of continuous radiation from electron–ion recombination and deflection of free electrons (bremsstrahlung radiation). A particularly interesting geochemical application of LIBS is the quantification of metals in ores at low ppm levels. Analysis of mine samples using conventional wet chemistry or fire assay techniques involves a lengthy sample preparation process and logistical waiting times of at least 24 h, resulting in production delays at mining or exploration sites [12]. LIBS can in principle provide quantitative results for a typical drill core within minutes without preparation. In particular, LIBS has been studied by our team for the quantification of gold [13–15] and palladium [16, 17] in solid ores where they are present in trace amounts, typically in the order of 1–10 ppm. Despite remarkable advances in the use of LIBS in geochemistry in recent years [7, 18–21], the understanding of the interaction between the laser and the solid rock surface is still very limited. This issue is further complicated by the fact that ores are typically composite media containing several different minerals on scales ranging from micrometers to centimeters. For example, in the case of palladium ore from the Lac des Iles (LDI) mine, we have identified about ten different minerals using a variety of microanalytical techniques (electron probe microanalysis, scanning electron microscope, and μ-XRF) and a database of LIBS spectra [19]. In its gabbronorite variety (of the same type as the ore sample studied here), this ore presents three main phases that occupy distinct areas of a few mm^2 on its surface, namely: (1) calcium-rich plagioclase feldspar (mainly bytownite), (2) amphibole (mainly hornblende), and (3) sulfides (mainly chalcopyrite, pentlandite, pyrrhotite and pyrite). In principle, the physical process of laser ablation and thus the amount of material ablated, is different for each minerall phase because they all have different compositions and physicochemical properties. Understanding laser-mineral interactions is relevant not only for practical applications on Earth, but also for extraplanetary exploration [22].

While laser ablation of rock samples for geochemical analysis has been little studied, ablation of materials by intense irradiation of laser pulses has been investigated in several other fundamental and applied fields [23, 24], particularly in analytical chemistry [25–27]. Since the first observation of laser ablation of a carbon rod in 1962 [28], laser ablation has been studied on many solid surfaces. The materials used include metals, semiconductors, dielectrics, ceramics and polymers [29]. The influence of laser parameters such as fluence [30, 31], pulse duration [32], laser spot size, number of laser shots [33], and wavelength [34] on crater morphology in different materials is still under investigation. The characterization of crater morphology has been mainly performed by methods such as scanning electron microscopy (SEM) [35], atomic force microscopy (AFM) [36], white light interferometry [37, 38], focused ion beam SEM (FIB-SEM) [39], optical microscopy [40], casting [41], and X-ray computed tomography [42].

Laser ablation is a complex process that depends on the nature of the material, the surrounding atmosphere, and the characteristics of the laser pulse [29]. Laser ablation is generally considered to result from a combination of photochemical processes, in which optically excited electrons lead directly to bond breakage, and photothermal processes, which lead to thermal bond breakage [43]. Photothermal processes are generally understood as the absorption of laser energy by free electrons through inverse bremsstrahlung and energy transfer from the hot electrons to the plasma and material [44]. The latter effect is favored by long laser pulses (>>1 ps) and long wavelength. LIBS typically uses near-infrared nanosecond pulses, such as those provided by Nd:YAG lasers, to generate hot plasmas with strong emission lines.

The aim of this work is to provide an overview of laser-mineral interactions in the context of LIBS geochemical analysis of ore samples with a focus on plasma characterization and laser ablation craters under ambient conditions in air at atmospheric pressure. For this purpose, we specifically selected a gabbronorite that is representative of the palladium ore from the LDI mine and whose palladium concentration has been quantified by LIBS [16] as well as by LIBS assisted with laser induced fluorescence (LIBS-LIF) [17]. The sample studied here was characterized by μ-XRF in order to clearly identify and map the main mineral phases where laser ablation was performed. We studied the laser ablation craters created on the surface of LDI ore samples for the three main mineral phases (plagioclase, amphibole, sulfides) for several series of laser shot numbers

(50, 250, 500 and 1000) using 2D images provided by the SEM and 3D profiles provided by an in-house optical coherence tomography (OCT) based system [45]. Although LIBS spectra can be obtained with a single laser shot [16], many laser shots are required to produce observable craters at the laser fluence and wavelength used, and thus to estimate the average amount of matter ablated per laser shot. The electron density and excitation temperature of the plasma were also estimated from the Fe and Ni emission lines of the LIBS spectra.

2 Materials and methods

2.1 Experimental setups

The experimental setup used for crater formation and LIBS spectra collection is schematically shown in Fig. 1. It basically consists of three elements: a laser, a spectrometer and a detector. The Nd:YAG laser used (CFR 200 from Quantel Laser by LUMIBIRD) can deliver pulse energies up to 200 mJ with a tunable repetition rate up to 20 Hz at a fundamental wavelength of 1064 nm, and with a full width at half maximum (FWHM) of the laser pulse time profile of 8 ns. The laser beam was focused on the rock surface by a 20 cm focal length lens. For the collection of LIBS spectra, the plasma emission was focused onto the circular input end of a fiber optic bundle consisting of twenty-five 100 µm diameter fibers. The vertically aligned output of this bundle was positioned in front of the entrance slit of a Czerny-Turner spectrometer (McPherson model 207) to match the pixel array of the intensified charge-coupled device (ICCD) (Istar DH720-25H-05, Andor Technology). The spectrometer has a focal length of approximately 0.67 m and a numerical aperture of F/5.8, covering wavelengths from 180 to 650 nm employing a UV-enhanced grating of 2400 grooves/mm. The corresponding reciprocal linear dispersion is approximately 12 pm/pixel at 267 nm. The spectrometer slit was set at 20 µm to obtain both good signal intensity and spectral resolution.

Before proceeding with the laser ablation experiments, we characterized the transverse energy distribution of the laser beam. For this purpose, we measured the laser beam in the focal plane of a plano-convex lens with a focal length of 250 mm at 1064 nm using an SP620U camera (with a pixel size of 4.4 µm × 4.4 µm) and the beam analysis software Ophir/Spiricon BeamGage. The 2D and 3D images of the energy profile are shown in Fig. 2. The beam has a circular shape with a diameter of approximately 750 µm at four standard deviations. The top of the beam contains some small speckles that form an overall slightly sloped profile.

The laser parameters used in this study are listed in Table 1. The laser energy was 80 mJ per pulse while the laser spot diameter on the target was 750 µm, resulting in a fluence of approximately 18 J cm^{-2} or an irradiance of 2.3 GW cm^{-2}. These parameters are the same as those optimized for the measurement of palladium concentration by LIBS in a previous study [16]. For LIBS signal acquisition, a delay time of 4 µs after the laser pulse (delay before signal integration starts) and a gate width of 10 µs (signal integration time) were used. These two values were chosen to obtain a near-optimal signal-to-noise ratio for our setup. All measurements were performed in air at atmospheric pressure with a laser repetition rate of 2 Hz, which is slow enough to avoid

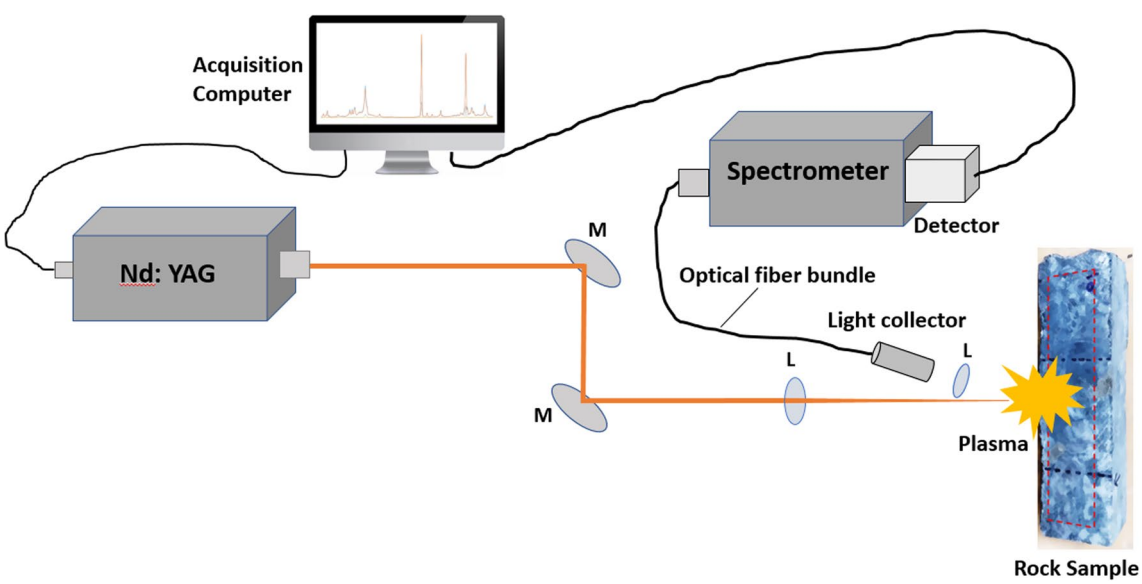

Fig. 1 Schematic representation of the LIBS experimental setup. Labels L and M refer to lens and mirror, respectively

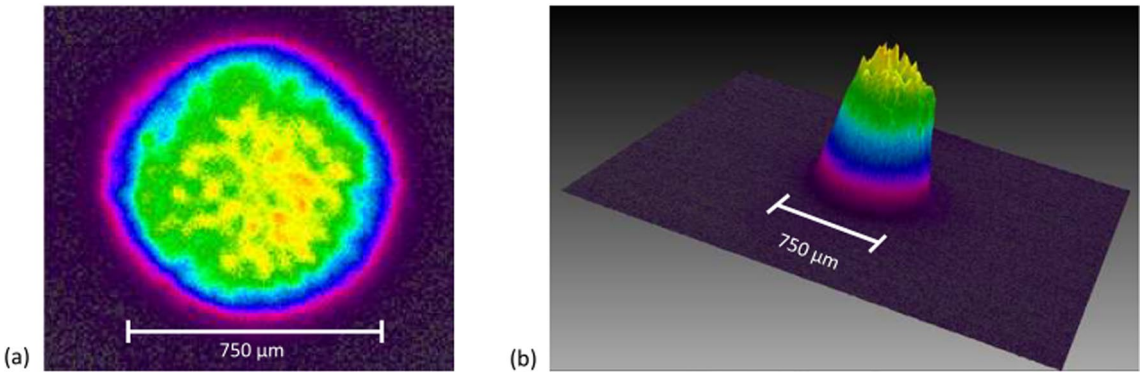

Fig. 2 Transverse energy profile of the laser beam. 2D profile (**a**) and 3D profile (**b**)

Table 1 LIBS parameters used for crater formation

Parameter	Value
Laser energy	80 mJ
Laser spot diameter	750 µm
Delay time	4 µs
Gate width	10 µs
Repetition rate	2 Hz
Spectrometer slit	20 µm

aerosols generated by previous laser shots. All measurements reported in this paper were performed within a few hours to minimize possible variations in configuration and atmospheric conditions.

The geochemical study was carried out using a µ-XRF M4 Tornado analyzer (Bruker GmbH, Germany). The µ-XRF analyzer is equipped with an Rh X-ray tube with a Be window, a polycapillary focusing optics, two silicon drift X-ray detectors (type SDD VH30P), a large sample chamber, and a motorized stage for sample positioning. The spot size of the incident X-ray beam was set to 20 µm and the acquisition time per pixel was 5 ms. The acquisition and processing of the µ-XRF data was performed using the software supplied with the instrument which allowed qualitative analysis (single and multi-element mapping) as well as quantification based on fundamental parameters (standardless) of the X-ray spectra [46]. For a selected area, a complete X-ray spectrum was acquired for each pixel within a grid. The multi-element distribution map provided information on the surface area distribution occupied by the mineral phases present in the scanned area.

2.2 Palladium ore sample

LIBS and µ-XRF analyses and laser ablation cratering were performed on a fragment of drill core from the LDI mine (Fig. 3). The LDI mine is located in the Mine Block Intrusion, 106 km northwest of Thunder Bay, Ontario, Canada. The LDI complex is a mafic to ultramafic intrusive complex and hosts significant PGE deposits [47]. The sample was collected from the B3 Zone deposit, which is hosted within the gabbronorite unit. The same surface was studied in [16] to illustrate a method for determining palladium content in ore using LIBS. This surface was also chosen for this study because of its exceptionally large, homogeneous, well-defined phase zones.

Half of the original one-meter drill core was analyzed by conventional methods. Its average elemental chemical content is summarized in Table 2. It can be seen that Si is the major constituent followed by Mg, Al, Ca and Fe. This table

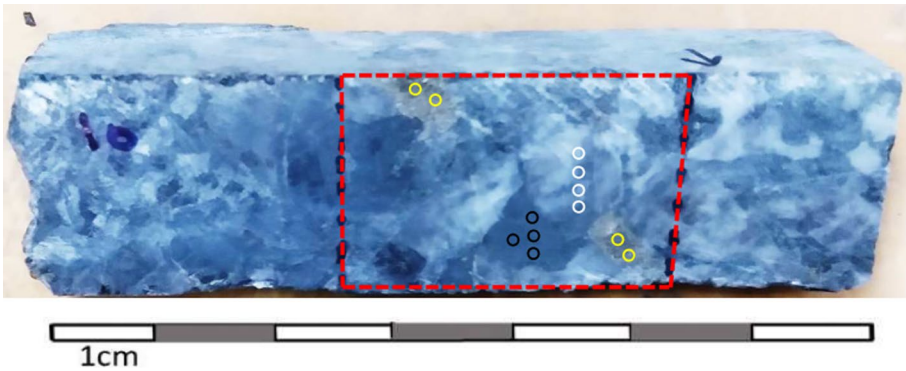

Fig. 3 Enhanced contrast photograph of the palladium ore sample analyzed in this study. The µ-XRF analysis was conducted in the area delineated by the red dashed lines. The approximate locations of the 12 craters examined in this study are indicated by circles in three different mineral phases: plagioclase feldspar (white circles), amphibole (black circles), and sulfides (yellow circles)

Table 2 Partial elemental chemical composition of the Lac des Iles drill core used in this study as determined by mine laboratory

Identification	Rock type	Elemental composition									
		Pt (ppm)	Pd (ppm)	Si (%)	Ca (%)	Fe (%)	S (%)	Cu (%)	Ni (%)	Al (%)	Mg (%)
18-805-X097924	Gabbronorite	0.568	4.93	24.2	6.6	4.7	0.35	0.14	0.31	7.7	7.8

is provided only to give a general idea of the elemental composition of the ore. As shown in Fig. 3, we focus instead on the analysis of the major mineral phases present in the ore.

3 Results and discussion

3.1 Mineralogical identification

A μ-XRF mineral identification procedure was carried out as described in our previous work [19]. Briefly, the multi-element map shown in Fig. 4 was first obtained. Then, the relative element concentrations provided by the instrument software were obtained at selected locations on the map (small triangles near the mineral labels in Fig. 4). The minerals were then identified by comparison with the generic formulas of the most likely minerals. Additional information from our previous study of samples of the same provenance was also employed. This included information from polarized light microscopy and electron probe microanalysis. The analysis confirmed the presence of minerals belonging to three different phases: amphibole, plagioclase and sulfides. Amphibole is mainly represented by hornblende (light pink zones), plagioclase by bytownite (blue zones) and sulfides by pyrrhotite, pentlandite, pyrite (deep pink and orange zones) and chalcopyrite (light green zones). The generic chemical composition of these minerals is given in Table 3, together with their mass density.

It should be noted that the mineral phases of rocks are rarely perfectly homogeneous, resulting in more complex compositions than those represented by their generic formulas. For example, electron probe microanalysis (EPMA) performed in our previous study on an ore of the same provenance (Supplementary Information of [19]) has shown the presence of a small amount of nickel and other metals in hornblende, which may be magnesium substitutes or micro-inclusions. Traces of iron were also found in bytownite. The presence of iron and nickel is clearly visible in the LIBS spectra of the three phases presented in Sect. 3.3, where their intense lines are used to determine plasma properties.

3.2 Cratering by laser ablation

Four craters were created at four different locations in each of the three main phases identified (plagioclase, amphibole, sulfides). Each crater was created with a different number of consecutive laser shots (50, 250, 500, 1000) at the same energy of 80 mJ per pulse and the same focal spot diameter of 750 μm. Photographs of the rock sample from Fig. 3, but with the actual craters, are shown in Fig. 5. Figure 5a shows the entire rock surface with the mineral phase boundaries drawn directly on the surface. The red dashed rectangle in

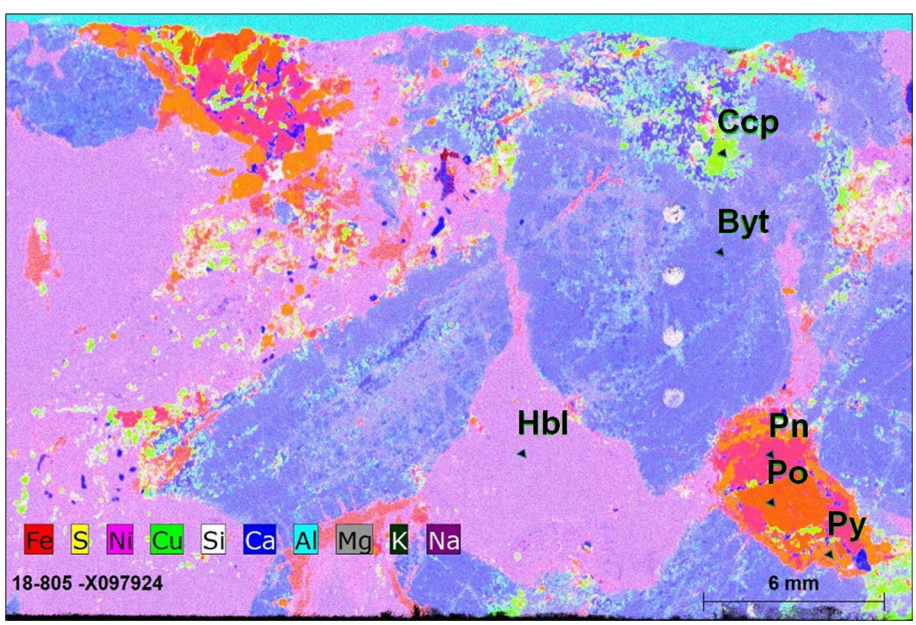

Fig.4 Combined μ-XRF elemental map of the area outlined by the red dashed lines in Fig. 3 with identification of some minerals at locations represented by small triangles: pyrite (Py), chalcopyrite (Ccp), bytownite (Byt), hornblende (Hbl), pentlandite (Pn) and pyrrhotite (Po). The four vertically aligned circles near the bytownite label are deep ablation craters produced on this phase. The other craters are not clearly visible on this map

Table 3 Results of semi-quantitative analysis for our LDI gabbronorite sample and corresponding mass density

Phase	Main mineral	Generic mineral formula	Mass density (g cm^{-3})
Amphibole	Hornblende (Hbl)	$(Ca, Na)_2 (Mg, Fe, Al)_5 (Al, Si)_8 O_{22} (OH)_2$	3.14
Plagioclase	Bytownite (Byt)	$(Ca_{0.7-0.9}Na_{0.3-0.1})$ $[Al(Al, Si)Si_2 O_8]$	2.71
Sulfides	Pyrrhotite (Po)	$Fe_{0.8-1.0}S$	4.61
	Pentlandite (Pn)	$(Ni, Fe)_9S_8$	4.80
	Chalcopyrite (Ccp)	$CuFeS_2$	4.19
	Pyrite (Py)	FeS_2	5.01

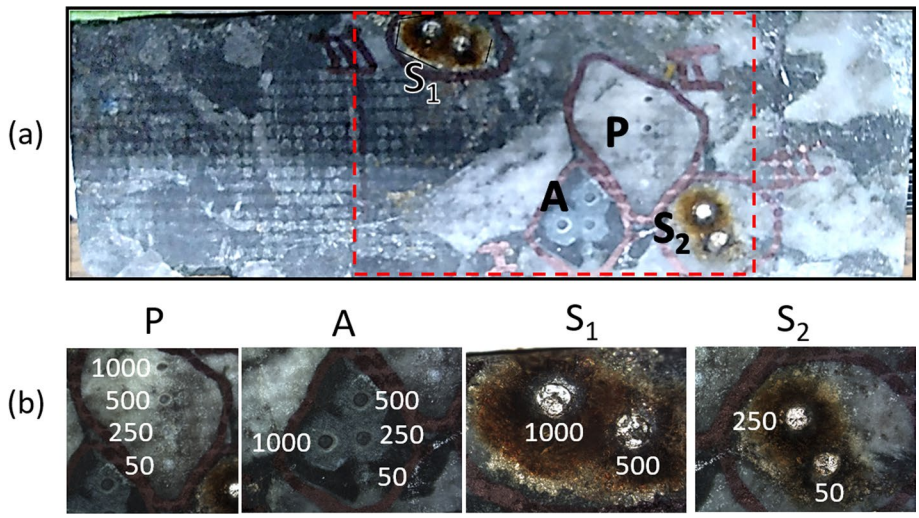

Fig. 5 Photographs of the rock fragment after cratering by laser ablation. **a** Photograph of the entire surface (see Fig. 3). The red dashed rectangle represents the area scanned by μ-XRF. **b** Magnification of the areas labeled P, A, S_1 and S_2 in (**a**). The P zone is plagioclase, the A zone is amphibole, and the S_1 and S_2 zones are sulfides. Crater labels indicate the number of laser shots at the same location

Fig. 5a corresponds to the area analyzed by μ-XRF (Fig. 4). Figure 5b magnifies the areas where the craters were formed. The number of laser shots corresponding to each crater is shown.

The craters look different in the three phases. In the sulfides (S_1 and S_2) a white metallic sheen appears at the bottom of the craters. This could be due to sulfur vaporization (sulfur vaporizes at 445 °C while iron vaporizes at ~ 3000 °C [48]), leaving a pure metallic phase (Fe, Ni, Cu) at the bottom of the crater. In addition, dark regions appear around the craters due to ejecta and oxidation reactions. Despite these transformations, the latter craters cannot be clearly identified on the μ-XRF map in Fig. 4. This is probably because the chemical changes due to ablation are below the absolute detection limit of μ-XRF. In amphibole (A), the craters appear as dark spots (except for the 50-shot crater) surrounded by a white rim and a larger white disk, which contrasts with the normal dark appearance of hornblende. These craters are also not visible on the μ-XRF map. In plagioclase (P), the craters appear as white or dark spots surrounded by a white rim, which are clearly visible on the μ-XRF map. The light color of the circular spots on the μ-XRF map suggests a chemical change that caused silicon to predominate at the bottom of the craters, probably a consequence of the high silicon content of bytownite and the high vaporization temperature (2355 °C) [48] of this element. As we will see from the OCT images, these craters are significantly deeper than those formed in the other phases.

SEM images at 300X magnification have been acquired with a FEI Inspect F50 instrument. Figure 6 shows two examples of craters for each of the three main phases: one obtained with 50 laser shots (first row) and one obtained with 1000 laser shots (second row). The craters produced in sulfides appear as solidified melt, consistent with the high metal content of this phase. Laser heating probably breaks the sulfur-metal bonds, leaving a pool of molten metal in the crater after the sulfur has evaporated. Crater diameters in this phase are close to 1 mm, significantly larger than the estimated laser spot size (750 μm). Amphibole shares with sulfide the appearance of a solidified melt, particularly evident in the 50-shot crater, while the 1000-shot crater has a more well-defined circular shape than in the sulfide phase. The crater diameter of 720 μm is similar to the laser spot size. In contrast, the bottom of the craters in plagioclase has a smoother but porous texture (note that the white spot in the 50-shot case and the black spot in the 1000-shot case are likely due to localized charge accumulation, as this material

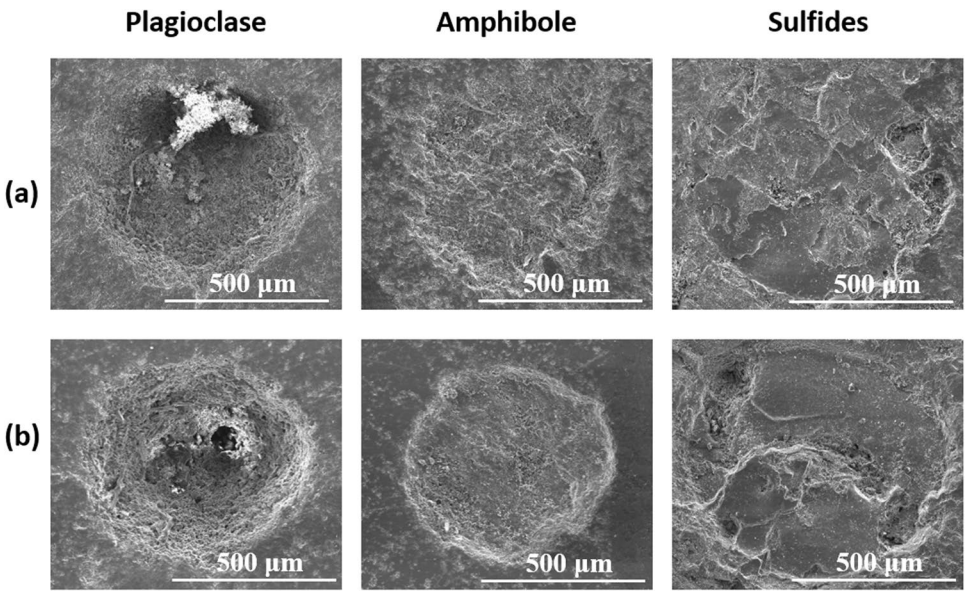

Fig. 6 300X SEM images obtained with secondary electrons that show laser ablation craters in the three main mineral phases for (**a**) 50 and (**b**) 1000 laser shots

has a low electrical conductivity). The crater diameters in this case are approximately 800 µm.

Images with lower resolution than SEM, but with 3D details, were obtained using the OCT technique. The OCT system used in this work was developed and operated at the National Research Council of Canada [45]. The results are shown in Fig. 7 for the three main mineral phases (columns) and for the four numbers of laser shots (rows). In these images, the overall surface tilt of a few degrees along the X and Y axes was compensated for by rotating the data, and the surface position $Z=0$ was determined by averaging the Z coordinates around the sides of each box.

Craters are much deeper in plagioclase (~700 µm per 1000 laser shots) compared to amphiboles and sulfides (less than 200 µm). In plagioclase, craters have a fairly regular truncated cone shape. For sulfides, the surface inside and outside the craters is highly undulating, suggesting melting of the material near the laser focus, consistent with the corresponding SEM images (Fig. 6), and possibly also migration of the material out of the crater. Amphibole shares many characteristics with sulfides in that the craters are shallow, and their interior surfaces are rather irregular, with the possible exception of the 1000 shot case. However, the area outside the crater is flatter than in sulfides.

Figure 7 also indicates the volumes of the craters calculated from the OCT data. The most accurate volume calculations are probably for the plagioclase craters due to their greater depth. In this phase, the volume appears to increase steadily with the number of laser shots and tends to be constant after about 250 laser shots. The saturation effect is most likely due to the decrease of the laser fluence (energy/surface) due to the increase of the effective interaction surface when the laser illuminates the inclined walls of the crater [49]. The defocusing of the laser as the crater deepens plays a minor role because the depth of field of the laser is greater than 2 mm. There appears to be a less consistent trend in the evolution of crater volume as a function of the number of laser shots in the amphibole. Given the shallowness of the craters, the accuracy of the volume calculation may not be sufficient to identify the true volume trend as a function of the number of laser shots. Volume calculations in sulfides are the least accurate because of the shallowness of the craters and the waviness of the surface around the laser focus, which makes it difficult to define the ground level $Z=0$. This surface condition can be explained by the melting of material around the crater, the ejection of molten material, and the formation of oxides. In fact, the sulfide phase is an aggregate of at least four sulfides in different proportions, each with different physical properties. This is in sharp contrast to plagioclase, which forms a single homogeneous crystal. Considering the first 50 laser shots, we can estimate the volume ablated per laser shot to be 10^{-4}–10^{-3} mm^3 in the three phases for the laser parameters used. Using the mass densities given in Table 3, we can estimate that the mass ablated by laser shot is approximately 1.25 µg for hornblende, 2.71 µg for bytownite, and between 1.68 and 2.00 µg for sulfides.

To rationalize our observations, we considered some thermodynamic properties of the mineral phases. According to the Bowen reaction series [50, 51], calcium-rich plagioclase feldspars such as bytownite have a higher melting temperature (~1400 °C) than amphibole (~900 °C). With respect to sulfides, pyrite is known to transform to pyrrhotite at temperatures as low as 743 °C. However, pyrrhotite melts at 1190 °C [52]. Pentlandite melts near 900 °C [53] while chalcopyrite melts at about 950 °C [48]. These values for

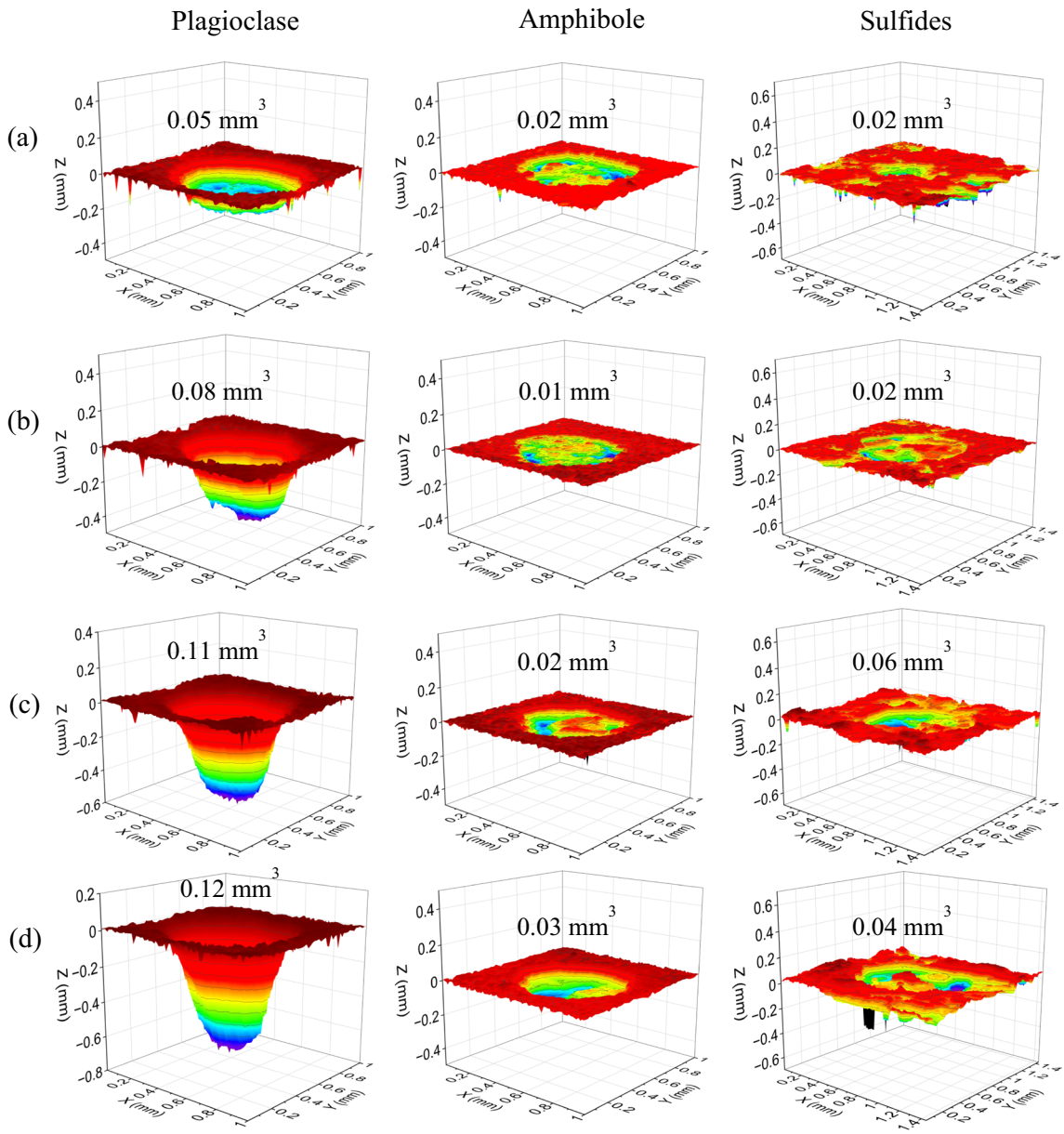

Fig. 7 OCT images of the ablation craters for the three main mineral phases and for different numbers of laser shots: 50 (**a**), 250 (**b**), 500 (**c**), and 1000 (**d**). The false colors correspond to the relative height of the craters from the bottom to the surface. Each crater profile is shown in a cube of 1 mm in length for plagioclase and amphibole, and 1.4 mm for sulfides. The calculated volume of each crater in mm^3 is indicated

sulfides are consistent with the amount of melt in and around laser-generated craters reported in [54]. These melting temperatures are generally consistent with the crater texture observed in SEM images (Fig. 6), which show that the texture of sulfide and amphibole craters resembles a solidified melt, in contrast to the plagioclase which is more smooth and porous. Although it was found in [55] that the ablated volume decreases with increasing melting temperature for Sn, Pb, Ni and Si, this relationship clearly does not hold in our case.

As we know, laser ablation is a complex process that involves several physicochemical properties of the material, as well as the interaction of the laser with the solid surface and with the plasma. Interestingly, in the present cases, there is an inverse correlation between the crater volumes and the thermal conductivity of the mineral phases. Thermal conductivity is lower in plagioclase (1.5–2.5 W m^{-1} K^{-1}) and higher in amphiboles (2.5–5.0 W m^{-1} K^{-1}), with the exact values depending on the phase

composition [56], and sulfides (19.2, 4.6, and 10.7 W m^{-1} K^{-1} for pyrite, pyrrhotite, and chalcopyrite, respectively) [57]. Thermal conductivity is known to play an important role in nanosecond pulse laser ablation, as high thermal conductivity generally means that more of the laser energy deposited on the surface is rapidly dissipated within the material, leaving less available for vaporization of the material at the surface [44]. A similar correlation between crater volume and thermal conductivity can be found in [39] where experiments were performed on polymers, Si, SiO_2 and Al. Thermal conductivity is also a critical parameter to understand the higher ablation efficiency of ultrashort laser pulses at a given fluence, since in this case the thermal loss of the energy absorbed at the surface to the body of the material does not have time to operate.

3.3 LIBS spectra and plasma properties

Additional characteristics of the laser ablation in the mineral phases of our sample are provided by the LIBS spectra as a function of the number of laser shots. The spectra shown in Fig. 8 were recorded in the 1000 shot crater of each phase. The spectral range was chosen around the Pd I line at 348.115 nm, which was used to determine the palladium content in [16] (the line is too small to be visible here). The spectral lines are dominated by the high emission elements iron and nickel. These elements are normal constituents of sulfides (Table 3). Iron is a normal component of hornblende, but nickel is less common. As mentioned above, iron and nickel are not normally present in bytownite, but can be found as traces in the form of micro-inclusions. Here we focus mainly on the Fe and Ni lines as we use them to determine plasma properties.

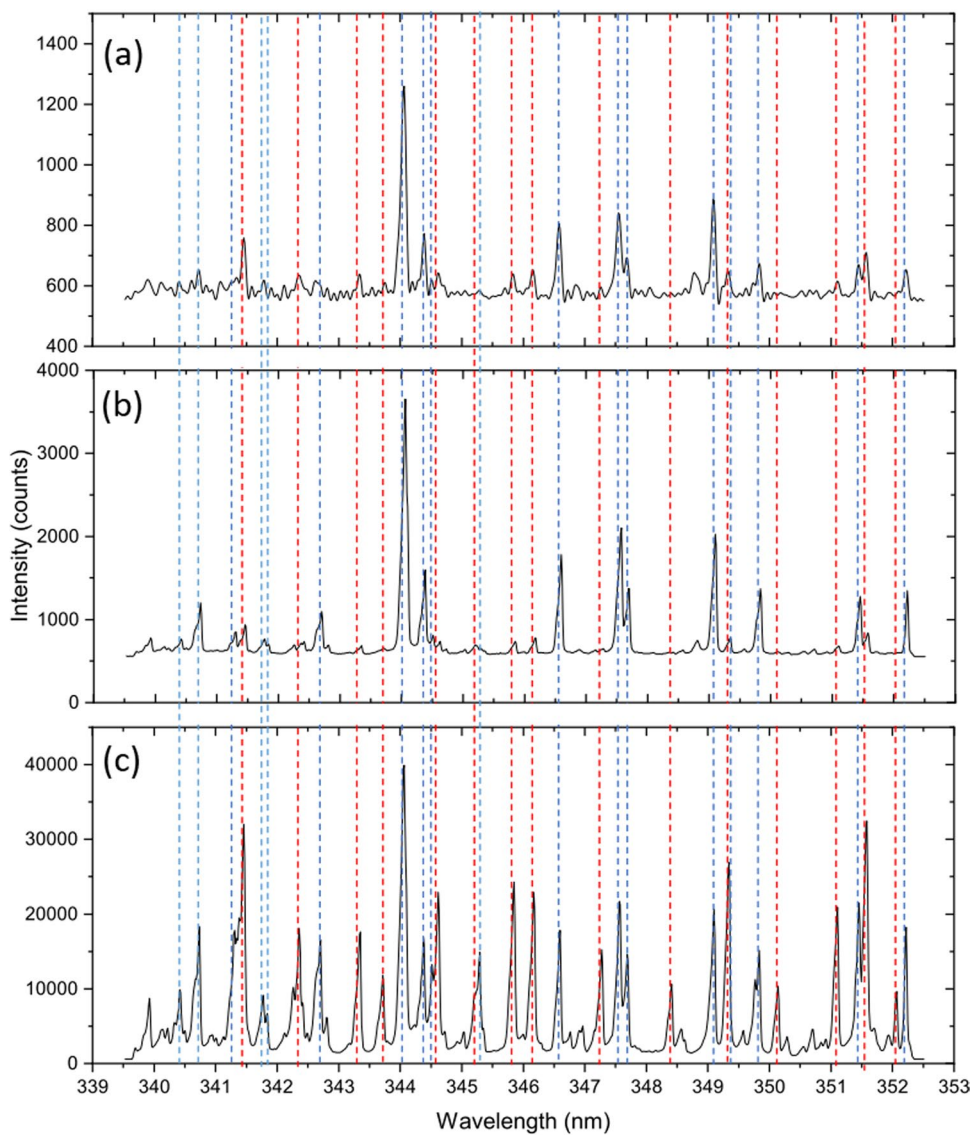

Fig. 8 Raw LIBS spectra between 339.5 nm and 352.5 nm for **a** plagioclase, **b** amphibole, and **c** sulfides for the 1000 laser shot craters. The spectra in (**b**) and (**c**) were obtained by averaging 100 spectra around laser shot numbers 500 and 100, respectively, while the spectrum in (**a**) was obtained by low-pass filtering of shot number 2. Vertical blue and red dashed lines correspond to Fe I lines (except for Fe II 349.35 nm) and Ni I lines, respectively

A striking feature of the spectra is the order of magnitude difference between the intensities of the lines in the different phases, which is related to the amount of iron and nickel they contain. The Fe and Ni lines were identified by comparison with the NIST LIBS database [58] with high line resolution for typical plasma parameters (temperature and electron density of 1 eV and 10^{17} cm^{-3}, respectively). All visible lines are Fe I and Ni I lines. The Fe II line at 349.35 nm should be visible but is strongly interfered with by the line at Ni I 349.30 nm.

Since LIBS is based on spectral lines, in Fig. 9 we consider the total plasma line content as a function of the number of laser shots at the same location. We define the total plasma line content as the area under the spectra after background subtraction. We observe that the line emission in amphibole and sulfides increases rapidly during the first few laser shots to reach a fairly constant regime after a few laser shots whereas in plagioclase the line emission decreases almost steadily by a factor of almost five between the second (highest line emission) and the last laser shot. After more than 300 shots, the plagioclase spectra are noisy, and no lines can be distinguished. The value of ~ 1 in Fig. 9 corresponds to random noise above the baseline. The reason for this phenomenon is related to the plateauing of the crater volume, which also occurs beyond the same number of laser shots (Fig. 7) and is due to the increase of the effective laser interaction area. This effect was also observed in [48]. Considering Fig. 9, the spectra shown in Fig. 8 were selected based on the optimal line content in each phase. Averages of 100 spectra were taken for amphiboles (laser shots 451–550) and sulfides (laser shots 51–150) to reduce noise. Such averaging was not possible for plagioclase due to the noisy spectra obtained after the first few laser shots, so the spectrum of laser shot number 2, which has the highest line content as shown in Fig. 9b, was selected, and the noise was reduced by low-pass filtering at 10 Hz. Figure 9b shows that a first cleaning laser shot increases the line intensity for the second shot.

We used the spectra in Fig. 8 to estimate the plasma electron excitation temperature and electron density in the three mineral phases. To determine the plasma electron excitation temperature, we selected Fe I lines with sufficient intensity and spectral resolution. Unfortunately, the Ni I lines in our spectral window have very close upper energy levels (between 3.61 and 3.83 eV), making them difficult to use for a Boltzmann plot. The Fe I lines, with their relevant parameters from NIST [59], are listed in Table 4. Note that none of these lines are resonant. The resulting Boltzmann plots are shown in Fig. 10. The highest electron temperature is obtained in sulfides, intermediate in amphibole, and lowest in plagioclase. This trend is consistent with the amount of ablated material reported in Sect. 3.2, since higher amounts of ablated material generally result in lower absorbed energy per electron. The temperatures obtained have values typical of those obtained in other materials for similar laser parameters, for example in an aluminum alloy for a delay of 4 µs [60]. Uncertainties in temperature were evaluated from the quality of the linear regression and from the uncertainties in A_{ki} and line intensity.

Table 4 Fe I lines used for the Boltzmann plots

Wavelength λ_{ki} (nm)	Degeneracy × Einstein coefficient $g_k A_{ki}$ (s^{-1}) (accuracy)	Upper energy level E_k (eV)
340.75	5.48×10^8 (10%)	5.81
342.71	4.54×10^8 (10%)	5.79
344.39	2.38×10^7 (10%)	3.69
346.59	3.37×10^7 (10%)	3.69
347.55	4.88×10^7 (10%)	3.65
347.67	1.72×10^7 (10%)	3.69

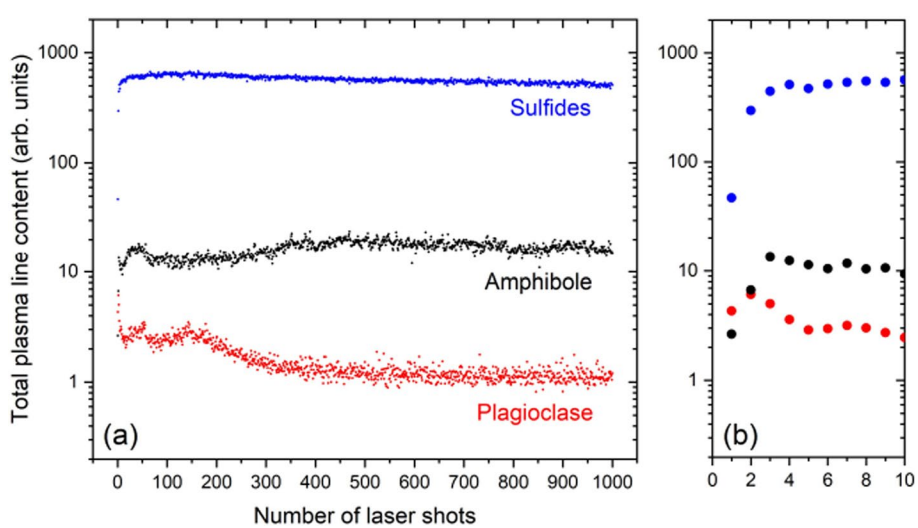

Fig. 9 Area under the spectra after background subtraction, highlighting the spectral line content, on a logarithmic scale, for the 1000 laser shot crater in plagioclase, amphibole, and sulfides. **a** All 1000 laser shots; **b** zoom from (**a**) to show the first 10 laser shots

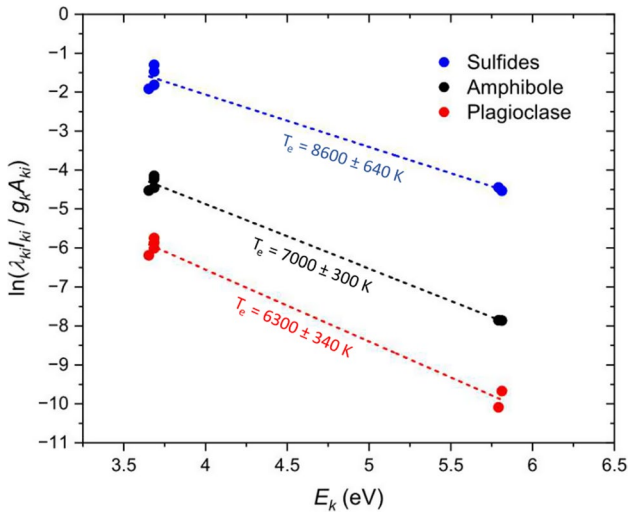

Fig. 10 Boltzmann plots with corresponding plasma electron temperature T_e for the three mineral phases

For the electron density, we used the isolated Ni I line at 346.166 nm (transition from 3.6060 to 0.0254 eV) for which the Stark broadening parameter has been measured [61]. We calculated the electron density from the expression

$$N_e \approx \frac{\Delta\lambda_{\mathrm{FWHM}}}{2\Delta\lambda_0}\left(\frac{T_e}{T_{e0}}\right)^{\frac{1}{2}} N_{e0}, \quad (1)$$

where $\Delta\lambda_0 = 5 \times 10^{-3}$ nm was measured at $N_{e0} = 6.6 \times 10^{16}$ cm^{-3} and $T_{e0} = 18{,}000$ K for the line of interest. T_e is the temperature shown in Fig. 10. The temperature factor is determined by theoretical considerations [62, 63]. By subtracting three pixels from the measured full width at half maximum of the line of interest ($\Delta\lambda_{\mathrm{FWHM}}$) to account for the instrument function, we obtained similar electron densities of $N_e \approx 2.0 \times 10^{17}$, 1.6×10^{17}, and 2.4×10^{17} cm^{-3} for plagioclase, amphibole, and sulfides, respectively. We estimate the uncertainties on $\Delta\lambda_{\mathrm{FWHM}}$ to be about 15%. These electron densities are close to the upper range of those obtained from minor element lines in an aluminum alloy using similar laser parameters and for a delay of 4 µs [60].

In order to consider any isolated line in our spectra, we also used Cowley's approximate broadening formula for neutral atoms [63] to obtain N_e from the measured $\Delta\lambda_{\mathrm{FWHM}}$,

$$\Delta\lambda_{\mathrm{FWHM}} \approx 1.54 \times 10^{-25} (n^*)^4 \lambda^2 N_e, \quad (2)$$

where λ is the wavelength of the line of interest (in nm) and n^* is the effective quantum number of the upper level. With $(n^*)^2 = 13.59/(I - E_k)$, where I is taken as the first ionization energy (in eV), we obtain for the Ni I 346.166 nm line similar values to those mentioned above, around $N_e = 2 \times 10^{17}$ cm^{-3}, for the three mineral phases. Almost the same values are obtained by considering the isolated Fe I 346.586 nm line (transition from 3.6864 to 0.1101 eV).

4 Conclusions

As LIBS gains popularity as a geochemical analytical technique due to the development of spectral databases and improved instrumentation, it has become pertinent to take a closer look at the effect of the laser on different mineral phases. In this work, we focused on the morphology and volume of laser-induced craters, as well as the plasma properties and emission spectra produced in the three main mineral phases of a palladium ore from the Lac des Iles mine: plagioclase, amphibole, and sulfides. We have shown, for the first time to our knowledge, that the characteristics of craters formed by laser ablation on a given ore sample can vary considerably from one phase to another for identical laser characteristics. This was made possible in particular by the OCT technique, which allows craters to be imaged in 3D. Since LIBS is a surface analysis technique, it was important to be able to answer the question of how much material is sampled with each laser shot and how this sampling differs from one mineral to another.

Regarding the morphology of the laser-generated craters, we produced a series of four craters in each phase with 50, 250, 500, and 1000 laser shots of 80 mJ each, with a focal spot of 750 µm in diameter. We observed them using SEM and OCT techniques, which provide high-resolution 2D and 3D images of the craters, respectively. The textures revealed by SEM appear as molten and resolidified materials for amphiboles and sulfides, and more uniform and porous for plagioclase, suggesting a different ablation mechanism than for the other two phases. Plagioclase craters are by far the deepest (~700 µm per 1000 laser shots vs < 200 µm for the other two phases) and have a truncated cone shape whereas for the other two phases the craters are shallow and generally indeterminate in shape. For plagioclase, the crater volume calculated from the OCT data tends to be constant as the number of laser shots increases due to the decrease in fluence as the laser interacts with the sloping crater walls. For the other two phases (especially sulfides), the evolution of the crater volume as a function of the number of laser shots is not as clear due to their shallow depth. Crater volume does not appear to be directly related to the melting temperature. However, thermal conductivity may be part of the physical interpretation of these observations. Considering the first 50 laser shots, the volume ablated per laser shot can be estimated to be 10^{-4}–10^{-3} mm^3 in the three phases for the laser parameters used, while the mass ablated is approximately 1.25 µg for hornblende, 2.71 µg for bytownite, and between 1.68 and 2.00 µg for sulfides.

Regarding the LIBS spectra and the associated plasma properties, we observed that the spectra are dominated by the strongly emitting species iron and nickel, although only traces of nickel are found in the studied sample and traces of iron in the plagioclase. In plagioclase, the spectral line content (integrated spectra with background subtracted) is maximal for the second laser shot. After a few hundred laser shots, the spectra are essentially random noise with no discernible spectral features. In contrast, for the other two phases, the maximum spectral line content is lower for the first laser shots and reaches a relatively stable value after a few laser shots. From these spectra, obtained at times greater than 4 µs, we extracted the plasma electron density and excitation temperature using the iron and nickel lines. The electron densities are quite similar for all three phases ($\sim 2 \times 10^{17}$ cm^{-3}). We obtained a lower electron temperature in plagioclase (~6300 K) than in amphibole (~7000 K) and sulfides (~8600 K).

This study is part of a larger project on the application of LIBS to the measurement of precious metals in rock ores. An extension of this work would be to focus on the variety of pyroxenite from the Lac des Iles ore, which contains a significant amount of phyllosilicate in addition to amphibole, plagioclase, and sulfides.

Acknowledgements We are grateful to Lionnel Djon from Impala Canada for providing us with quarter drill cores from the Lac des Iles mine and their laboratory analysis, as well as for the financial support of Impala Canada. Suzie Côté of the Université Laval is thanked for the operation and data acquisition of both the SEM and the µ-XRF instruments. We also acknowledge the professional work of Guy Lamouche of the National Research Council of Canada (NRC) who carried out the OCT measurements. This work was primarily supported by the National Science and Engineering Research Council of Canada (NSERC) [Grant Number STPGP 521608-18].

Author contributions SS: data collection, software, writing. IE: data collection, software. NM: preparation of reference samples and the multi-element map. PB: preparation of the experimental setup. MC: funding acquisition and supervision, MS: methodology and supervision, FV: funding acquisition, supervision, and project administration.

Data availability The data are available from the corresponding author on request.

Declarations

Conflict of interest The authors declare that they have no known competing financial interests or personal relationships that could have appeared to influence the work reported in this paper.

Open Access This article is licensed under a Creative Commons Attribution 4.0 International License, which permits use, sharing, adaptation, distribution and reproduction in any medium or format, as long as you give appropriate credit to the original author(s) and the source, provide a link to the Creative Commons licence, and indicate if changes were made. The images or other third party material in this article are included in the article's Creative Commons licence, unless indicated otherwise in a credit line to the material. If material is not included in the article's Creative Commons licence and your intended use is not permitted by statutory regulation or exceeds the permitted use, you will need to obtain permission directly from the copyright holder. To view a copy of this licence, visit http://creativecommons.org/licenses/by/4.0/.

References

1. J.D. Winefordner, I.B. Gornushkin, T. Correll, E. Gibb, B.W. Smith, N. Omenetto, Comparing several atomic spectrometric methods to the super stars: special emphasis on laser induced breakdown spectrometry, LIBS, a future super star. J. Anal. At. Spectrom. **19**, 1061–1083 (2004)
2. D.A. Cremers, L.J. Radziemski, *Handbook of Laser-Induced Breakdown Spectroscopy*, 2nd edn. (John Wiley & Sons, Chichester, 2013)
3. A.W. Miziolek, V. Palleschi, I. Schechter (eds.), *Laser Induced Breakdown Spectroscopy* (Cambridge University Press, Cambridge, 2006)
4. R.S. Harmon, R.E. Russo, R.R. Hark, Applications of laser-induced breakdown spectroscopy for geochemical and environmental analysis: a comprehensive review. Spectrochim. Acta Part B. **87**, 11–26 (2013)
5. R.S. Harmon, C.J.M. Lawley, J. Watts, C.L. Harraden, A.M. Somers, R.R. Hark, Laser-induced breakdown spectroscopy—an emerging analytical tool for mineral exploration. Minerals **9**, 718 (2019)
6. R.S. Harmon, G.S. Senesi, Laser-induced breakdown spectroscopy–a geochemical tool for the 21st century. Appl. Geochem. **128**, 104929 (2021)
7. F.F. Fontana, B. van der Hoek, S. Tassios, C. Tiddy, J. Stromberg, N. Francis, Y.A. Uvarova, D.G. Lancaster, Laser Induced Breakdown Spectroscopy (LIBS) for whole rock geochemistry. J. Geochem. Explor. **246**, 107160 (2023)
8. C. Fabre, Advances in Laser-Induced Breakdown Spectroscopy analysis for geology: a critical review. Spectrochim. Acta Part B. **166**, 105799 (2020)
9. B. Lemière, R.S. Harmon, *XRF LIBS for Field Geology*, vol. 20 (Wiley, 2021), pp.1046–1173
10. G.E. De Benedetto et al., Infrared spectroscopy in the mineralogical characterization of ancient pottery. J. Cult. Herit. **3**, 177–186 (2002)
11. O.V. Borisov, X. Mao, R.E. Russo, Effects of crater development on fractionation and signal intensity during laser ablation inductively coupled plasma mass spectrometry. Spectrochim. Acta Part B. **55**, 1693–1704 (2000)
12. B. Nguegang Kamwa, K. Rifai, M. Laflamme, M. Constantin, M. Castello, F. Vidal, P. Bouchard, K. Fytas, A. Blouin and M. Sabsabi, Sampling strategy by statistical analyses of LIBS data in the context of a portable gold analyser, Tenth International Mining Geology Conference, Hobart, Tasmania, 20–22 September 2017.
13. A. Harhira, P. Bouchard, K. Rifai, J. El Haddad, M. Sabsabi, A. Blouin, M. Laflamme, Advanced Laser-induced breakdown spectroscopy (LIBS) sensor for gold mining. In Proceedings of the Conference of Metallurgists (COM), Vancouver, BC, Canada, 27–30 (2017)
14. K. Rifai, M. Laflamme, M. Constantin, F. Vidal, M. Sabsabi, A. Blouin, P. Bouchard, K. Fytas, M. Castello, B. NguegangKamwa, Analysis of gold in rock samples using laser-induced breakdown spectroscopy: matrix and heterogeneity effects. Spectrochim. Acta Part B. **134**, 33–41 (2017)
15. I. Elhamdaoui, K. Rifai, J. Iqbal, N. Mohamed, S. Selmani, J. Fernandes, P. Bouchard, M. Constantin, M. Laflamme, M. Sabsabi, F. Vidal, Measuring the concentration of gold in ore samples by laser-induced breakdown spectroscopy (LIBS) and comparison

with the gravimetry/ atomic absorption techniques. Spectrochim. Acta Part B. **183**, 106256 (2021)
16. S. Selmani, N. Mohamed, I. Elhamdaoui, J. Fernandes, P. Bouchard, M. Constantin, M. Sabsabi, F. Vidal, Laser-induced breakdown spectroscopy analysis of palladium in rock ore. Spectrochim. Acta Part B. **196**, 106523 (2022)
17. I. Elhamdaoui, N. Mohamed, S. Selmani, P. Bouchard, M. Sabsabi, M. Constantin, F. Vidal, Rapid quantitative analysis of palladium in ores using Laser-Induced Breakdown Spectroscopy assisted with laser-induced fluorescence (LIBS-LIF). J. Anal. At. Spectrom. **37**, 2537 (2022)
18. K. Rifai, F. Doucet, L. Ozcan, F. Vidal, LIBS core imaging at kHz speed: paving the way for real-time geochemical applications. Spectrochim. Acta Part B. **150**, 43–48 (2018)
19. N. Mohamed, K. Rifai, S. Selmani, M. Constantin, F. Doucet, L. Ozcan, M. Sabsabi, F. Vidal, Chemical and mineralogical mapping of platinum-group element ore samples using laser-induced breakdown spectroscopy and micro-X-ray fluorescence. Geostand. Geoanal. Res. **45**, 539–550 (2021)
20. C. Fabre, D. Devismes, S. Moncayo, F. Pelascini, F. Trichard, A. Lecomte, B. Bousquet, J. Cauzid, V. Motto-Ros, Elemental imaging by laser-induced breakdown spectroscopy for the geological characterization of minerals. J. Anal. At. Spectrom. **33**, 1345–1353 (2018)
21. K. Kuhn, J.A. Meima, D. Rammlmair, C. Ohlendorf, Chemical mapping of mine waste drill cores with laser-induced breakdown spectroscopy (LIBS) and energy dispersive X-ray fluorescence (EDXRF) for mineral resource exploration. J. Geochem. Explor. **161**, 72–84 (2016)
22. A. Fau, O. Beyssac, M. Gauthier, P.Y. Meslin, A. Cousin, K. Benzerara, S. Bernard, J.C. Boulliard, O. Gasnault, O. Forni, R.C. Wiens, M. Morand, P. Rosier, Y. Garino, S. Pont, S. Maurice, Pulsed laser-induced heating of mineral phases: Implications for laser-induced breakdown spectroscopy combined with Raman spectroscopy. Spectrochim. Acta Part B. **160**, 105687 (2019)
23. A.A. Bol'shakov, J.H. Yoo, C. Liu, J.R. Plumer, R.E. Russo, Laser-induced breakdown spectroscopy in industrial and security applications. Appl. Opt. **49**, C132 (2010)
24. D. Bäuerle, *Laser Processing and Chemistry*, 3rd edn. (Springer, Berlin, 2011)
25. R.E. Russo, T.W. Suen, A.A. Bol'shakov, J. Yoo, O. Sorkhabi, X. Mao, J. Gonzalez, D. Oropeza, V. Zorba, Laser plasma spectrochemistry. J. Anal. At. Spectrom. **26**, 1596 (2011)
26. R.E. Russo, X. Mao, J.J. Gonzalez, V. Zorba, J. Yoo, Laser ablation in analytical chemistry. Anal. Chem. **85**, 6162–6177 (2013)
27. C. Neff, P. Keresztes Schmidt, P.S. Garofalo, G. Schwarz, D. Günther, Capabilities of automated LA-ICP-TOFMS imaging of geological samples. J. Anal. At. Spectrom. **35**, 2255 (2020)
28. G.C. Dacey, Optical masers in science and technology. Science **135**, 3498 (1962)
29. D.W. Bauerle, *Laser Processing and Chemistry* (Springer, Berlin, 2011)
30. T.U. Rahman, Z.U. Rehman, S. Ullah, H. Qayyum, B. Shafique, R. Ali, U. Liaqat, A.H. Dogar, A. Qayyum, Laser-induced plasma-assisted ablation (LIPAA) of glass: effects of the laser fluence on plasma parameters and crater morphology. Opt. Laser Technol. **120**, 105768 (2019)
31. M. Akram, S. Bashir, M.S. Rafique, A. Hayat, K. Mahmood, Laser induced surface morphology of molybdenum correlated with breakdown spectroscopy. Plasma. Chem. Plasma Process. **37**, 287–304 (2017)
32. E. Terasawa, T. Shibuya, D. Satoh, Y. Moriai, H. Ogawa, M. Tanaka, R. Kuroda, Y. Kobayashi, K. Sakaue, M. Washio, Pulse duration dependence of ablation threshold for fused silica in the visible femtosecond regime. Appl. Phys. A **126**, 446 (2020)
33. M.E. Shaheen, J.E. Gagnon, B.J. Fryer, Excimer laser ablation of aluminum: influence of spot size on ablation rate. Laser Phys. **26**, 116102 (2016)
34. H. Mustafa, D.T.A. Matthews, G.R.B.E. Römer, Wavelength dependence of picosecond-pulsed laser ablation of hot-dip galvanized steel. Appl. Phys. A **128**, 296 (2022)
35. S.M. Eggins, L.P.J. Kinsley, J.M.G. Shelley, Deposition and element fractionation processes during atmospheric pressure laser sampling for analysis by ICP-MS. Appl. Surf. Sci. **278**, 127–129 (1998)
36. D.J. Hwang, H. Jeon, C.P. Grigoropoulos, J. Yoo, R.E. Russo, Femtosecond laser ablation induced plasma characteristics from submicron craters in thin metal film. Appl. Phys. Lett. **91**, 251118 (2007)
37. R.E. Russo, X. Mao, H. Liu, J. Gonzalez, S.S. Mao, Laser ablation in analytical chemistry—a review. Talanta **57**, 425–451 (2002)
38. J.J. Gonzalez, A. Fernandez, D. Oropez, X. Mao, R.E. Russo, Femtosecond laser ablation: experimental study of the repetition rate influence on inductively coupled plasma mass spectrometry performance. Spectrochim. Acta Part B. **63**, 277–286 (2008)
39. D. Bigoni, M. Milani, R. Jafer, C. Liberatore, S. Tarazi, L. Antonelli, D. Batani, Influence of mechanical and thermal material properties on laser-produced crater-morphology and their study by focused ion beam & scanning electron microscope imaging. J. Laser Micro/Nanoeng. **5**, 169 (2010)
40. A. Casal, R. Cerrato, M.P. Mateo, G. Nicolas, 3D reconstruction and characterization of laser induced craters by in situ optical microscopy. Appl. Surf. Sci. **374**, 271–277 (2016)
41. V. Grimaudo, P. Moreno-García, A. Cedeño López, A. Riedo, R. Wiesendanger, M. Tulej, C. Gruber, E. Lörtscher, P. Wurz, P. Broekmann, Combining anisotropic etching and PDMS casting for three-dimensional analysis of laser ablation processes. Anal. Chem. **90**, 2692–2700 (2018)
42. D. Monserrat Lopez, V. Grimaudo, G. Prone, A. Flisch, A. Riedo, R. Zboray, T. Lüthi, M. Mayor, M. Fussenegger, P. Broekmann, P. Wurz, E. Lörtscher, Automated, 3-D and sub-micron accurate ablation-volume determination by inverse molding and x-ray computed tomography. Adv. Sci. **9**, 2200136 (2022)
43. T. Lippert, Laser application of polymers. Adv Polym Sci **168**, 51 (2004)
44. S. Laville, F. Vidal, T.W. Johnston, O. Barthélemy, M. Chaker, B. Le Drogoff, J. Margot, M. Sabsabi, Fluid modeling of the laser ablation depth as a function of the pulse duration for conductors. Phys. Rev. E. **66**, 066415 (2002)
45. V. Detalle, M. Dufour, J-P Monchalin, M. Sabsabi**,** L. St-Onge, Method and apparatus for 3-dimensional compositional mapping of heterogeneous materials. Publication date: May **22** (2003). https://worldwide.espacenet.com/patent/search/family/025533595/publication/US2003095266A1?q=pn%3DUS2003095266A1. Accessed in Aug 25, 2023.
46. S. Flude, M. Haschke, M. Storey, Application of benchtop micro-XRF to geological materials. Mineral. Mag. **81**, 923–948 (2017)
47. D. Decharte, C. Perusse, T. Hofton, C. Roney, G. Marrs, S. Taylor, S. Olson, D. Thibodeau, D. Peck and B. Young, Feasibility study for Lac des Iles Mine incorporating underground mining of the Roby Zone. Technical Report, North American Palladium Ltd. **889** (2018)
48. https://cameo.mfa.org/wiki/Category:_Materials_database, Cameo Materials Database. Accessed in Aug 25, 2023.
49. A. Borisov, H. Palme, Solubilities of noble metals in Fe-containing silicate melts as derived from experiments in Fe-free systems. Am. Miner. **85**, 11–12 (2000)
50. N.L. Bowen, The reaction principle in petrogenesis. J. Geol. **30**, 177–198 (1922)

51. D. Perkins et al., Mineralogy, LibreText geosciences. https://geo.libretexts.org/Bookshelves/Geology/Mineralogy_(Perkins_et_al.). Accessed in Aug 25, 2023.
52. P.J. Sylvester, A practical guide to platinum-group element analysis of sulphides by laser-ablation ICPMS, in *Chapter 13. Laser-ablation-ICPMS in the earth sciences. Principles and applications*. ed. by P. Sylvester (Mineralogical Association of Canada, Ottawa, 2001)
53. G. Kullerud, Thermal stability of pentlandite. Can. Mineral. **7**(3), 353–366 (1963)
54. S.E. Gilbert, L.V. Danyushevsky, K. Goemann, D. Death, Fractionation of sulphur relative to iron during laser ablation-ICP-MS analyses of sulphide minerals: implications for quantification. J. Anal. At Spectrom. **29**, 1024–1033 (2014)
55. K. Amponsah-Manager, N. Omenetto, B.W. Smith, I.B. Gornushkin, J.D. Winefordner, Microchip laser ablation of metals: investigation of the ablation process in view of its application to laser-induced breakdown spectroscopy. J. Anal. At. Spectrom. **20**, 544–551 (2005)
56. G. Dalla Santa, A. Galgaro, R. Sassi, M. Cultrera, P. Scotton, J. Mueller, D. Bertermann, D. Mendrinos, R. Pasquali, R. Perego, S. Pera, E. Di Sipio, G. Cassiani, M. De Carli, A. Bernardi, An updated ground thermal properties database for GSHP applications. Geothermics **85**, 101758 (2020)
57. E.H. Braye, A.H. Sehon, B.B. Darwent, Thermal decomposition of sulfides. J. Am. Chem. Soc. **77**, 5282–5285 (1955)
58. https://physics.nist.gov/PhysRefData/ASD/LIBS/libs-form.html for Nist LIBS Database. Accessed in August 25, 2023.
59. https://physics.nist.gov/PhysRefData/ASD/lines_form.html for Atomic Spectra Database. Accessed in August 25, 2023.
60. V. Detalle, R. Héon, M. Sabsabi, L. St-Onge, An evaluation of a commercial Echelle spectrometer with intensified charge-coupled device detector for materials analysis by laser-induced plasma spectroscopy. Spectrochim. Acta Part B. **56**, 1011–1025 (2001)
61. N. Konjevic, A. Lesage, J.R. Fuhr, W.L. Wiese, Experimental stark widths and shifts for spectral lines of neutral and ionized atoms (A Critical Review of Selected Data for the Period 1989 Through 2000). J. Phys. Chem. Ref. Data. **31**, 819 (2002)
62. M.C. Artu, Parametric estimates of line broadening due to quadratic or linear Stark effect, Spectroscopic challenges in photoionized plasmas. ASP Conf. Ser. **246**, 155 (2001)
63. C.R. Cowley, An approximate Stark broadening formula for use in spectrum synthesis. The Observatory. **91**, 139–140 (1971)

Publisher's Note Springer Nature remains neutral with regard to jurisdictional claims in published maps and institutional affiliations.